

Uncovering the role of thermal inertia in establishing the seasonal Arctic warming pattern

Sergio A. Sejas^{1*}, Patrick C. Taylor²

¹Science Systems and Applications, Inc, Hampton, VA 23666, USA.

²Climate Science Branch, NASA Langley Research Center, Hampton, VA 23681, USA.

* Corresponding Author: Sergio A. Sejas

Email: sergio.sejas@nasa.gov

<https://orcid.org/0000-0003-4139-3499>

Classification

Physical Sciences: Earth, Atmospheric, and Planetary Sciences

Keywords

Arctic Warming; Thermal Inertia; Sea Ice Loss; Seasonal Pattern; Heat Capacity

Author Contributions

S. A. Sejas conceived the idea for this study, downloaded the data, and performed the calculations. S. A. Sejas and P. C. Taylor discussed the results throughout the whole process and were responsible for the writing of the manuscript.

This PDF file includes:

Main Text
Figures 1 to 6
Supplementary Information

Abstract

The observed and projected Arctic warming pattern is characterized by an early winter maximum and a summer minimum. While a robust feature of Arctic climate change, the seasonal expression of surface warming remains incompletely understood. Previous explanations attribute the seasonality to surface energy budget changes induced by climate feedbacks. However, these hypotheses cannot explain key features of the simulated seasonal structure: seasonal heating rate changes and the early winter warming maximum. We find that the increase in the thermal inertia of the Arctic system due to the transition from a lower thermal inertia surface (sea ice cover) to a higher thermal inertia surface (ice-free ocean) captures these key seasonal features. Our analysis shows that the early winter Arctic warming maximum results from a slowing of the background surface cooling rate from summer to winter, not from an additional net energy input into the Arctic surface during that time.

Significance Statement

Arctic warming and its seasonal pattern are salient features of climate projections; yet, an understanding of process drivers and sources responsible for its large inter-model spread remain unclear. We find that the substantial increase in the thermal inertia of the Arctic surface during fall and winter establishes the seasonal Arctic warming pattern. The transition from a lower thermal inertia surface (sea ice) to one with significantly higher thermal inertia (ocean) slows the cooling rate of the surface from summer to winter, magnifying Arctic warming during fall and winter. Differences in model-projected thermal inertia changes explain a substantial portion of the inter-model winter warming uncertainty indicating fall thermal inertia variations are a key source of predictability for the Arctic winter climate.

Introduction

In response to the anthropogenic increase of greenhouse gases, observations and climate projections indicate that the Arctic surface warms more rapidly than any other region on Earth (1–7), termed Arctic amplification (AA). However, AA does not manifest evenly throughout the year, instead it exhibits a pronounced seasonality—minimum in summer and maximum in early winter (2, 8–11). Accurate projection of this seasonal structure is important because it dictates a seasonally dependent impact on climate system dynamics and on human and ecological systems (12–14). Additionally, the largest uncertainty in Arctic warming projections coincides with the early winter warming maximum (5, 10, 11). Assessing the causes of this uncertainty and constraining the inter-model spread in Arctic warming requires a better understanding of the mechanisms and physical processes responsible for the seasonal warming pattern.

Varying explanations for the seasonal Arctic warming pattern have been proposed. Many studies (1, 6, 15–18) argue that sea ice decline and the associated energy flux response drives the seasonal Arctic warming pattern. Sea ice decline, through a reduction of the surface albedo, increases the solar energy absorbed by the surface (i.e., the surface albedo feedback) in summer, but studies argue that the additional energy first melts sea ice before weakly warming the surface, explaining the warming minimum in summer (1, 16, 18). Sea ice decline, on the other hand, contributes to the maximum fall/winter warming by facilitating an increase of sensible and latent heat fluxes, known as the ice-thickness or ice insulation feedback (1, 6, 18). While the increase in sensible and latent heat fluxes contributes to the warming of the lower atmosphere, this energy perturbation represents a transfer of energy from the surface to the atmosphere that suppresses surface warming (8–

11). Other studies suggest that an increase in wintertime downwelling longwave (LW) radiation accounts for the enhanced Arctic warming in fall and winter (8, 15). The increase in downwelling LW radiation is attributed to lower tropospheric warming by the surface turbulent fluxes, an increase of polar clouds (9, 10), and an increase of poleward heat and moisture transport (4, 19–21). A few studies also suggest that the weaker Planck feedback (a smaller increase in LW emissions per unit of warming) at colder temperatures also contributes to the Arctic seasonal warming pattern (5, 10).

While providing various physical interpretations of the seasonal Arctic warming pattern, the aforementioned studies all assert that energetics explain the seasonality of Arctic warming. Alternatively, changes in thermal inertia represent a viable pathway to explain the seasonal Arctic warming pattern. Different surfaces (e.g., sea ice vs. ice-free ocean) have different specific heat capacities and layer depths over which the surface interacts with the atmosphere, yielding different thermal inertias. These different thermal inertias have varying effects on the climate system including the lagged response between the ocean surface temperature and seasonal variations in sunlight (22). The thermal inertia of the global ocean is also responsible for the timescale of the global temperature response to anthropogenic forcing and the differences between the transient and equilibrium climate response (23).

Substantial thermal inertia changes are possible and projected to occur in the Arctic as sea ice surfaces convert to ice-free ocean. Using a simple energy balance climate model, Robock (24) diagnoses the individual influences of snow area, sea ice area, snow albedo, and sea ice albedo on the Arctic surface temperature response to a 1% increase and decrease in solar insolation. The results indicate that changes in thermal inertia resulting from sea

ice area changes, termed the ice thermal inertia feedback, dominate the seasonal surface temperature change pattern, and not the associated energy flux changes.

The potentially significant role that thermal inertia changes play in the Arctic has been somewhat overlooked by investigations into the energy flux changes resulting from climate feedbacks, including some of our own work (9, 11). Applying principles motivated by Robock (24), the current study investigates the influence of thermal inertia changes on the seasonal Arctic surface warming pattern in CMIP5 RCP8.5 climate change simulations of the late 21st century. Our analysis stratifies the seasonal warming by Arctic surface type (land, ice-free ocean, and sea ice regions), quantifies the seasonality of surface energy flux changes in the Arctic, and decomposes the contributions to the seasonal surface skin temperature heating rate change.

Our results illustrate that thermal inertia changes are a significant contributor to the seasonal Arctic warming pattern and provide a new explanation for the early winter maximum warming. Specifically, the early winter Arctic surface warming maximum results from a slowing of the background surface cooling rate from summer to winter, not from an additional energy input into the Arctic surface during that time period. Equipped with this new knowledge, we demonstrate that fall changes in thermal inertia, using both surface heating rate and sea ice decline as proxies, explain the CMIP5 maximum winter warming inter-model spread. Thus, an improved understanding of process contributions to thermal inertia change will help reduce the uncertainty in Arctic winter warming projections.

Results

Surface Type Dependence of Arctic Warming Seasonality

Different surface types (e.g., sea ice vs. ice-free ocean) have different specific heat capacities; the specific heat capacity of sea water, for example, is ~2 times larger than that of sea ice. In addition, the depth of the layer over which a surface interacts with the atmosphere varies substantially between sea ice (~10 cm (25, 26)) and ocean (~50 m (27)) with significant consequences for thermal inertia. Cumulatively, this means that the effective surface heat capacity is on the order of 1000 times greater for ocean than sea ice. As a result, the seasonal variations in surface skin temperature (T_S) and the surface skin temperature heating rate ($\frac{dT_S}{dt}$) are expected to vary from one surface type to another.

Stratifying the Arctic by surface type (sea ice, ocean, and land), within the historical climate (see Methods), indicates a stronger T_S annual cycle and seasonal ΔT_S pattern for locations with sea ice relative to the other surface types. In the historical (late 20th century climate) and RCP8.5 (late 21st century climate) simulations (Figure 1a-c), T_S shows a robust annual cycle for each surface type where the maximum T_S occurs earlier in the summer for sea ice and land surfaces compared to ice-free ocean, whose maximum is delayed due to its larger thermal inertia. Considering the surface temperature changes between the historical climate and the projected late 21st century climate, Figs. 1d-f demonstrate the differences in the magnitude and seasonality of the warming pattern between surface types. Though all surface types exhibit similar warming during summer, the greatest surface warming occurs for locations covered by sea ice in the historical climate in early winter, meaning sea ice grid points experience the most pronounced

seasonality (Fig. 1d). Land grid points (Fig. 1f) also show a maximum warming during early winter, but less pronounced. Ice-free ocean grid points warm the least and exhibit very little seasonal variation (Fig. 1e). Thus, the Arctic ΔT_S warming amplitude and seasonal pattern are predominantly attributed to grid points that experience sea ice loss. This hints at the importance of thermal inertia changes on the seasonal Arctic warming pattern, since grid points that experience sea ice loss are the only regions that undergo a substantial change in thermal inertia.

The surface skin temperature seasonal heating rate, $\frac{\partial T_S}{\partial t}$, is dependent on two factors, namely the net surface energy flux and the effective surface heat capacity (i.e., surface thermal inertia). Surface type dependent changes in $\frac{\partial T_S}{\partial t}$ further point to the significant role of thermal inertia. Stratifying $\frac{\partial T_S}{\partial t}$ by surface type, as before, shows a similar seasonal structure between sea ice (Fig. 2a) and land (Fig. 2c) but a different seasonal structure for ocean (Fig. 2b), consistent with the surface type dependence on thermal inertia. Changes to the seasonal heating rate ($\Delta \frac{\partial T_S}{\partial t}$) are caused by changes to the net surface energy flux or thermal inertia of the surface. We find sea ice grid points exhibit the largest $\Delta \frac{\partial T_S}{\partial t}$ values relative to other Arctic grid points (Fig. 2d-f). Despite exhibiting a similar $\frac{\partial T_S}{\partial t}$ seasonal structure to land in the historical simulation, sea ice grid points have a more pronounced seasonal $\Delta \frac{\partial T_S}{\partial t}$ pattern than land because of the substantial changes in thermal inertia due to the transition from sea ice to sea water. During fall and winter the seasonal heating rate for sea ice increases at twice the rate as that of land for all models ($\sim 4 \text{ K month}^{-1}$ vs. $\sim 2 \text{ K month}^{-1}$ in the ensemble average). Ice-free ocean grid points exhibit small $\Delta \frac{\partial T_S}{\partial t}$

values year-round, largely due to their large thermal inertia. The primary difference between the three surface types is the large thermal inertia increase that occurs only for sea ice grid points as sea ice melts and converts to ice-free ocean.

The surface type stratification of $\Delta \frac{\partial T_S}{\partial t}$ (Fig. 2d-f) provides evidence that the large thermal inertia increase contributes to the asymmetric seasonal pattern of Arctic surface warming. For a given net energy flux input, a surface with a larger (smaller) thermal inertia experiences a smaller (larger) surface heating rate. For sea ice grid points, the thermal inertia increase reduces the surface cooling rate ($\Delta \frac{\partial T_S}{\partial t} > 0$) during fall and winter (Fig. 2d), which slows the seasonal T_S cooling from summer to winter. As a result, the surface in these regions warms in fall and early winter relative to the historical simulation (Fig. 1d). During spring and summer, the thermal inertia increase reduces the surface warming rate ($\Delta \frac{\partial T_S}{\partial t} < 0$) slowing the seasonal warming from winter to summer, which suppresses ΔT_S in spring and summer (Fig. 1d).

The influence of thermal inertia on the asymmetric seasonal warming pattern is evident at the grid box scale as well. The strong area-weighted spatial correlations in Fig. 3 indicate that grid boxes with a larger decrease in sea ice concentration (SIC) experience a greater slowdown of the seasonal cooling rate in fall and winter and also warm more; this is the case for each model across the ensemble. In spring, the positive correlation indicates that grid boxes with a greater thermal inertia increase exhibit a greater slowdown of the seasonal surface warming. We see a weaker positive correlation in spring (Fig. 3a) between ΔSIC and $\Delta \frac{\partial T_S}{\partial t}$ than the negative correlation in fall, in part due to the smaller SIC decline in spring (Fig. S1). The fact that sea ice grid boxes with a greater SIC decline (i.e. larger

thermal inertia increase) also exhibit a larger reduction in the cooling rate and a larger warming supports the explanation that the amplification of the fall and winter surface warming occurs in response to increased thermal inertia.

Contributions to the Seasonal Arctic Surface Heating Rate

We hypothesize that the thermal inertia increase in response to decreased SIC plays a key role in determining the seasonal pattern of $\Delta \frac{\partial T_s}{\partial t}$ and as a result the seasonal pattern of Arctic warming. To test our hypothesis, we quantify the individual contributions to $\Delta \frac{\partial T_s}{\partial t}$. Using the mosaic approach, the T_s of a sea ice grid box is given by the weighted average of the two surface types,

$$T_s = SST * (1 - SIC) + T_{s,ice} * SIC \quad (1).$$

Hence the heating rate is given by,

$$\frac{\partial T_s}{\partial t} = \frac{\partial SST}{\partial t} * (1 - SIC) + \frac{\partial T_{s,ice}}{\partial t} * SIC + (T_{s,ice} - SST) * \frac{\partial SIC}{\partial t} \quad (2),$$

where SST is sea surface temperature and $T_{s,ice}$ is sea ice surface temperature. Applying a first-order Taylor series expansion to the change of Eq. 2 between the current and future climates yields

$$\Delta \left(\frac{\partial T_s}{\partial t} \right) \approx \left[\underbrace{\left(\frac{\partial T_{s,ice}}{\partial t} - \frac{\partial sst}{\partial t} \right) * \Delta SIC}_{I} + \underbrace{SIC * \Delta \left(\frac{\partial T_{s,ice}}{\partial t} \right)}_{II} + \underbrace{(1 - SIC) * \Delta \left(\frac{\partial sst}{\partial t} \right)}_{III} + \underbrace{(T_{s,ice} - sst) * \Delta \left(\frac{\partial SIC}{\partial t} \right)}_{IV} + \underbrace{\frac{\partial SIC}{\partial t} * \Delta (T_{s,ice} - sst)}_{V} \right] \quad (3).$$

The expression in Eq. 3 decomposes $\Delta \frac{\partial T_s}{\partial t}$ into contributions from changes in SIC, $T_{s,ice}$, sst , and their respective rates of change. The decomposition depicts the model-simulated $\Delta \frac{\partial T_s}{\partial t}$ accurately with a small residual as indicated by the close match between the true

ensemble mean total (dashed red line in Fig. 4a) and the diagnosed total (solid red line in Fig. 4a). More importantly, it allows us to isolate and quantify the impact of the thermal inertia increase due to the surface conversion from sea ice to sea water (i.e., ΔSIC ; term I) on the seasonal pattern of $\Delta \frac{\partial T_S}{\partial t}$.

ΔSIC (Fig. 4b; term I) significantly contributes to $\Delta \frac{\partial T_S}{\partial t}$ and reaches rates of +2 K month⁻¹ in October and November and -1.5 K month⁻¹ in May and June. The ΔSIC term directly reflects the slowing of both the background seasonal cooling during fall/winter and seasonal warming during spring/summer associated with the thermal inertia increase.

The decomposition analysis also reveals that $\Delta \frac{\partial T_{s,ice}}{\partial t}$ (term II) is an important contributor to $\Delta \frac{\partial T_S}{\partial t}$. Figure 4c shows the contributions from $\Delta \frac{\partial T_{s,ice}}{\partial t}$ are approximately +2 K month⁻¹ in October and November and -2.0 K month⁻¹ in January through June. This term physically indicates that the background $\frac{\partial T_{s,ice}}{\partial t}$ cooling rate slows in fall and warming rate slows from winter to early summer. Figure 4d, alternatively, illustrates that $\Delta \frac{\partial T_S}{\partial t}$ attributed to $\Delta \frac{\partial sst}{\partial t}$ (term III) contribute minimally to the $\Delta \frac{\partial T_S}{\partial t}$. The larger changes in $\Delta \frac{\partial T_{s,ice}}{\partial t}$ versus $\Delta \frac{\partial sst}{\partial t}$ are rooted in the smaller thermal inertia of sea ice versus ocean. Figure 5e and 5f show the contributions from $\Delta \frac{\partial SIC}{\partial t}$ (term IV) and $\Delta(T_{s,ice} - sst)$ (term V), respectively. While these terms make non-negligible individual contributions in winter months, they largely cancel and neither term aligns well with the overall $\Delta \frac{\partial T_S}{\partial t}$ seasonal

pattern. Overall, the decomposition analysis indicates that the ΔSIC and $\Delta \frac{\partial T_{s,ice}}{\partial t}$ terms account for most of the $\Delta \frac{\partial T_S}{\partial t}$ term.

The $\Delta \frac{\partial T_{s,ice}}{\partial t}$ (term III) seasonal pattern must be driven by changes in the net surface energy flux over sea ice portions of a grid box as the thermal inertia of sea ice experiences relatively little change. Figure 5 summarizes changes in the surface energy budget terms for sea ice grid boxes. The surface energy budget changes show increases in upward sensible and latent heat fluxes and upward LW fluxes (Fig. 5a-c) during fall and winter, which cool the surface, as well as an increase in downward LW fluxes (Fig. 5d) that warm the surface. Overall, the net changes in the surface energy budget (Fig. 5f) indicate a stronger cooling of the surface in fall and winter that is inconsistent with the increase of $\Delta \frac{\partial T_{s,ice}}{\partial t}$ (Fig. 4c). The available CMIP5 output does not allow us to differentiate the surface energy flux changes over the sea ice and ocean portions of an individual grid box. Explaining the diagnosed values of $\Delta \frac{\partial T_{s,ice}}{\partial t}$ requires that models produce markedly different surface energy flux changes over the sea ice and ocean portions of these individual grid boxes (see Discussion).

Relationship between Maximum Surface Temperature Change and Heating Rate Change

In the previous section, the decomposition analysis illustrated the influence of changes in thermal inertia on $\Delta \frac{\partial T_S}{\partial t}$. These changes in $\Delta \frac{\partial T_S}{\partial t}$ affect the seasonal Arctic surface warming pattern by slowing the surface cooling and warming rates during the transitions from summer to winter and winter to summer, respectively. The slowing of the surface cooling during fall to early winter means the amplitude of Arctic warming grows in time

from summer to early winter reaching a maximum in early winter. Similarly, the slowing of the surface warming during spring and summer means the amplitude of Arctic warming decreases seasonally from winter to summer, reaching a minimum in summer. Considering fall and winter, the result implies that a larger thermal inertia increase should correspond to a larger early winter warming maximum. Thus, if the role of thermal inertia is significant then it should serve as a reliable predictor of the simulated change in winter warming.

We investigate the importance of the thermal inertia change on winter warming by quantifying the correspondence between ΔSIC and the projected $\Delta \frac{\partial T_S}{\partial t}$ during fall and early winter (SOND) across the CMIP5 model ensemble. The results indicate that ΔSIC is an important factor controlling $\Delta \frac{\partial T_S}{\partial t}$ in fall/early winter. Figure 6a shows a strong correlation ($r=-0.70$) between ΔSIC and $\Delta \frac{\partial T_S}{\partial t}$ in SOND illustrating that models simulating a larger SIC decline also simulate a larger slowdown of the fall/early winter cooling rate. Furthermore, both ΔSIC and $\Delta \frac{\partial T_S}{\partial t}$ in SOND exhibit a strong negative ($r=-0.82$; Fig. 6b) and positive ($r=0.92$; Fig. 6c) correlation, respectively, with the maximum wintertime surface warming. Therefore, models with a larger SIC decline and slowdown of the cooling rate in SOND simulate a larger maximum wintertime surface warming. Alternatively, SOND changes in the net surface energy flux show a much weaker correspondence with the projected maximum wintertime temperature increase and are anti-correlated ($r=-0.47$; Fig. 6d), which is contrary to expectations if net energy flux changes are responsible for the warming. We note that our net surface energy flux change calculation excludes the contribution of ocean heat transport. However, it is unlikely changes in ocean heat transport would be large enough to change the sign of the correlation. While we were unable to

directly assess the contribution of ocean heat transport to changes in net surface energy flux, a recent study (10) indicates that ocean heat transport changes make a small contribution to the net surface energy flux changes. As a result, we do not expect the contribution of ocean heat transport to substantially modify the picture provided in Fig. 6. The differing thermal inertia increases between models therefore accounts for most of the inter-model winter warming spread.

Discussion

Our explanation differs from previous work that asserts that surface energy flux changes due to climate feedbacks solely explain the seasonality of Arctic surface warming. Supported by our analysis, we argue that the thermal inertia change due to the transition from sea ice to sea water is the principal factor driving the asymmetric seasonal pattern of Arctic surface warming and its dependence on surface type. This mechanism drives the early winter maximum Arctic surface warming by slowing the background surface cooling rate from summer to winter, establishing maximum warming in early winter. The thermal inertia feedback represents a change in the surface temperature sensitivity to energy fluxes that impacts the seasonal magnitude of Arctic warming. Conversely, we argue that it is the annual mean increase in surface energy fluxes that enhances the absorption of energy by the surface and is responsible for the long-term warming of the Arctic.

Despite this separation of roles between climate feedbacks that cause surface energy budget perturbations and the thermal inertia feedback, they are inextricably linked. For example, the slowing of the fall and early winter cooling rate in areas of sea ice loss, by the thermal inertia feedback, warms the surface and enhances the surface-to-air temperature gradient, which increases the upward LW flux and the upward turbulent heat

fluxes. The thermal inertia feedback mainly operates via changes in SIC. Therefore, any climate feedback (SAF, clouds, etc.) that affects the evolution of SIC can influence the character of the thermal inertia feedback. Based upon the importance of fall/early winter thermal inertia changes on the projected winter warming maximum (Fig. 6), surface energy budget perturbations due to climate feedbacks in fall are important for the thermal inertia feedback by delaying the sea ice freeze onset. For instance, recent studies indicate that an increase in Arctic low clouds, in response to sea ice reductions, has the potential to enhance downward LW radiation at the surface and delay fall freeze onset. In addition, an increase in downward LW radiation due to enhanced fall/early winter heat and moisture transport by the atmosphere could also delay fall sea ice freeze onset (11, 20, 21). Thus, the representation of clouds and atmospheric energy transports in fall/early winter could play a significant role in modulating the seasonal warming pattern through the thermal inertia feedback by delaying fall sea ice freeze onset. Similarly, oceanic heat transports have also been found to influence the timing of fall sea ice freeze onset (28). However, the strongest coupling is likely between the SAF and thermal inertia feedback.

The coupling between the SAF and thermal inertia feedback can be explained as a feedback loop involving seasonal variations of sea ice. Considering an arbitrary starting point, the SAF and thermal inertia feedback coupling begins with the slowing of the surface cooling rate in fall to early winter by the thermal inertia feedback, leading to thinner winter/spring sea ice and the early winter warming maximum. Thinner sea ice is more vulnerable to melting-out and uncovering the darker ocean underneath leading to a larger SAF in spring and summer. A larger SAF warms the sea surface and produces a warmer summer SST maximum. A warmer SST maximum means it will take longer to reach the

freezing point, delaying the fall sea ice freeze onset. The delay in the fall sea ice freeze onset indicates a decline in SIC, which strengthens the thermal inertia feedback. This interaction continues as long as sea ice remains and represents an amplifying (i.e., positive) feedback loop that not only establishes the seasonal Arctic warming pattern but is a dominant contributor to Arctic warming amplification. The strong positive coupling between the two (Fig. S2a) explains why SAF, which is only effective in spring and summer, correlates well with the winter warming maximum (Fig. S2b). It also explains why fixing surface albedo to a constant, while allowing the sea ice concentration to decline, greatly reduces the magnitude of Arctic warming (16); however, the seasonal Arctic warming pattern remains the same (Fig. 2 in (16)) since the thermal inertia feedback is still triggered by the sea ice decline caused by the greenhouse forcing and other climate feedbacks. Sea ice decline therefore amplifies Arctic warming through the SAF but establishes the seasonal Arctic warming pattern through its impact on the thermal inertia of the Arctic surface. In addition, sea ice extent is more important for the thermal inertia feedback than sea ice thickness because the presence of sea ice reduces the thermal inertia of the surface. Overall, the decline in SIC fundamentally controls both the SAF and the thermal inertia feedback and therefore represents the most important metric for Arctic climate change.

Our decomposition analysis reveals that sea ice temperature is an equally important contributor to $\Delta \frac{\partial T_s}{\partial t}$. However, as shown in Fig. 5, the surface energy flux changes over sea ice grid boxes do not support the model simulated $\Delta \frac{\partial T_{s,ice}}{\partial t}$. Reconciling this result demands different surface energy flux responses over the remaining sea ice and uncovered (i.e.,

ocean) portions of the sea ice grid boxes. While an analysis of these differences is not possible using the CMIP5 archived output, we speculate on the implied changes. During fall and winter, we expect weaker changes to the surface turbulent fluxes over sea ice than over the uncovered portions of the grid boxes, which would result in a less negative net surface energy flux perturbation. An additional positive energy flux input may also come from the oceanic heat flux from below (29) as thinner sea ice means the sea ice surface is less insulated from the warmer ocean below. These possible explanations warrant future investigation as they could strongly influence the seasonally asymmetric Arctic sea ice surface skin temperature response.

Consistent with previous studies, the surface air temperature displays the same seasonal Arctic warming pattern (Fig. S3a) as the surface skin temperature (ΔT_S), and also exhibits a very similar change to its seasonal heating rate (Fig. S3b). Unlike ΔT_S , the surface air temperature change cannot be explained by a change in the surface air heat capacity and thermal inertia. The similarities, however, are not surprising since the surface skin and air temperatures are tightly coupled through latent and sensible heat fluxes and through thermal-radiative coupling (30). The ΔT_S and $\Delta \frac{\partial T_S}{\partial t}$ are generally greater (in magnitude) than their respective counterparts for surface air, particularly in fall and winter, indicating the coupling between the two is driven by the surface skin warming. Since the seasonal cooling from summer to winter slows more for the surface skin than surface air temperature, the surface-to-air temperature difference increases, which leads to stronger upward sensible and latent heat fluxes in fall and winter (Fig. 5). This upward latent and sensible heat flux increase contributes to the large fall/winter Arctic surface air temperature

warming. Additionally, the warmer surface skin temperatures enhance the upward LW radiation emitted by the Arctic surface (Fig. 5), warming the surface air through enhanced absorption in the lower atmosphere. It is through these increases in upward energy flux, in regions of sea ice loss, that the warming signal of the surface is imprinted to the lower atmosphere.

In closing, the correspondence between fall/early winter Δ SIC and maximum winter warming via the thermal inertia feedback points to the importance of accurately representing the evolution of fall sea ice extent. The changes in fall SIC and the timing of fall sea ice freeze onset are important metrics for Arctic Amplification. Thus, an improved understanding and modeling of the factors that influence fall/early winter sea ice extent (e.g., sea ice physics, ocean mixed layer depth, surface energy budget, atmospheric variability etc.) are needed to produce more reliable simulations of maximum Arctic surface warming. For example, a recent study (31) shows that CMIP5 intermodel differences in sea ice loss can be traced to differences in the simulation of seasonal growth and melt in the present climate, which relate to the background sea ice thickness. Another study (11) found that climate models simulate a wide range of present-day values and projected changes in mixed layer depth in the Arctic that impact the effective heat capacity of the surface. Our results indicate that proxies of thermal inertia change (such as Δ SIC and $\Delta \frac{\partial T_s}{\partial t}$) explain the intermodel spread in maximum winter warming and can potentially be used to constrain projections of Arctic Amplification. We see significant potential for using observations of fall thermal inertia, sea ice extent, and fall freeze onset to constrain projected winter warming and reduce uncertainty in projected Arctic Amplification.

Methods

In this study, we analyze data from state-of-the-art atmosphere-ocean general circulation model (Table S1) participants in the 5th phase of the Coupled Model Intercomparison Project (CMIP5). Specifically, two types of CMIP5 experiments(32) are used: 1) Historical simulations (1850-2005) with time-varying forcing consistent with observations, and 2) representative concentration pathway 8.5 (RCP8.5) climate simulations (2006-2100) that simulate a future climate with radiative forcing reaching $\sim 8.5 \text{ W m}^{-2}$ by year 2100. The CMIP5 data are derived from the monthly mean outputs of the Historical and RCP8.5 model simulations produced by the Coupled Model Intercomparison Project Version 5 (CMIP5), which are archived and freely accessible at <http://data.ceda.ac.uk/badc/cmip5/data/cmip5/> and <https://esgf-node.llnl.gov/search/cmip5/>. For each model monthly mean surface skin and air temperatures, surface downwelling and upwelling shortwave fluxes, surface downwelling and upwelling longwave fluxes, and surface upward sensible and latent heat fluxes on its native atmospheric grid are obtained, while sea ice concentration, sea-ice surface temperature, and sea surface temperature on its native ocean grid are also obtained. Monthly mean climatological values of these variables are calculated by averaging 30 years in the historical simulations (1976-2005) and RCP8.5 simulations (2071-2100). Climatological changes of these variables are determined by subtracting the historical values from the RCP8.5 values. For the climatological seasonal heating rate calculation, the yearly month-to-month temperature changes (i.e., Jan-Dec, Feb-Jan, Mar-Feb, etc.) were calculated prior to taking the climatological average.

Arctic (60N-90N) grid points are divided into land, ocean, and sea ice surface types using the historical climatology. All atmospheric grid variables are interpolated to their corresponding ocean grid for each model analyzed to be able to separate oceanic grid points from land grid points, and to further decompose oceanic grid points into those that have sea ice concentration values greater than zero in the historical climate (i.e., sea ice grid points) and those that are ice-free. Both a forward and backward first order Taylor expansion of Eq. 3 for sea ice grid points was carried out, whose mean was used to produce the results in Fig. 4.

Acknowledgments

S. A. Sejas' research was supported by an appointment to the NASA Postdoctoral Program at the NASA Langley Research Center, administered by Universities Space Research Association under contract with NASA. P. C. Taylor is supported by the NASA CERES Project and by the NASA Interdisciplinary Studies Program grant NNH12ZDA001N-IDS. We acknowledge the World Climate Research Programme's Working Group on Coupled Modelling, which is responsible for CMIP, and we thank the climate modeling groups (listed in Table S1 of this paper) for producing and making available their model output. For CMIP the U.S. Department of Energy's Program for Climate Model Diagnosis and Intercomparison provides coordinating support and led development of software infrastructure in partnership with the Global Organization for Earth System Science Portals.

References

1. J. A. Screen, I. Simmonds, The central role of diminishing sea ice in recent Arctic temperature amplification. *Nature* **464**, 1334–1337 (2010).
2. M. M. Holland, C. M. Bitz, Polar amplification of climate change in coupled models. *Clim. Dyn.* **21**, 221–232 (2003).
3. S. Manabe, R. T. Wetherald, The Effects of Doubling the CO₂ Concentration on the climate of a General Circulation Model. *J. Atmospheric Sci.* **32**, 3–15 (1975).
4. M. Cai, Dynamical greenhouse-plus feedback and polar warming amplification. Part I: A dry radiative-transportive climate model. *Clim. Dyn.* **26**, 661–675 (2006).
5. F. Pithan, T. Mauritsen, Arctic amplification dominated by temperature feedbacks in contemporary climate models. *Nat. Geosci.* **7**, 181–184 (2014).
6. M. C. Serreze, A. P. Barrett, J. C. Stroeve, D. N. Kindig, M. M. Holland, The emergence of surface-based Arctic amplification. *The Cryosphere* **3**, 11–19 (2009).
7. V. Ramanathan, M. S. Lian, R. D. Cess, Increased atmospheric CO₂: Zonal and seasonal estimates of the effect on the radiation energy balance and surface temperature. *J. Geophys. Res. Oceans* **84**, 4949–4958 (1979).
8. J. Lu, M. Cai, Seasonality of polar surface warming amplification in climate simulations. *Geophys. Res. Lett.* **36**, L16704 (2009).
9. S. A. Sejas, *et al.*, Individual Feedback Contributions to the Seasonality of Surface Warming. *J. Clim.* **27**, 5653–5669 (2014).
10. A. Laîné, M. Yoshimori, A. Abe-Ouchi, Surface Arctic Amplification Factors in CMIP5 Models: Land and Oceanic Surfaces and Seasonality. *J. Clim.* **29**, 3297–3316 (2016).
11. R. C. Boeke, P. C. Taylor, Seasonal energy exchange in sea ice retreat regions contributes to differences in projected Arctic warming. *Nat. Commun.* **9**, 5017 (2018).
12. E. Post, *et al.*, Ecological Dynamics Across the Arctic Associated with Recent Climate Change. *Science* **325**, 1355–1358 (2009).
13. J. G. Ernakovich, *et al.*, Predicted responses of arctic and alpine ecosystems to altered seasonality under climate change. *Glob. Change Biol.* **20**, 3256–3269 (2014).

- 460 14. L. Xu, *et al.*, Temperature and vegetation seasonality diminishment over northern
461 lands. *Nat. Clim. Change* **3**, 581–586 (2013).
- 462 15. R. Bintanja, E. C. van der Linden, The changing seasonal climate in the Arctic. *Sci.*
463 *Rep.* **3**, 1556 (2013).
- 464 16. A. Hall, The role of surface albedo feedback in climate. *J. Clim.* **17**, 1550–1568
465 (2004).
- 466 17. R. G. Graversen, M. Wang, Polar amplification in a coupled climate model with
467 locked albedo. *Clim. Dyn.* **33**, 629–643 (2009).
- 468 18. S. Manabe, R. J. Stouffer, Sensitivity of a global climate model to an increase of
469 CO₂ concentration in the atmosphere. *J. Geophys. Res. Oceans* **85**, 5529–5554
470 (1980).
- 471 19. J. Lu, M. Cai, Quantifying contributions to polar warming amplification in an
472 idealized coupled general circulation model. *Clim. Dyn.* **34**, 669–687 (2010).
- 473 20. S. Lee, T. Gong, S. B. Feldstein, J. A. Screen, I. Simmonds, Revisiting the Cause of
474 the 1989–2009 Arctic Surface Warming Using the Surface Energy Budget:
475 Downward Infrared Radiation Dominates the Surface Fluxes. *Geophys. Res. Lett.*
476 **44**, 10,654–10,661 (2017).
- 477 21. B. Luo, D. Luo, L. Wu, L. Zhong, I. Simmonds, Atmospheric circulation patterns
478 which promote winter Arctic sea ice decline. *Environ. Res. Lett.* **12**, 054017 (2017).
- 479 22. D. L. Hartmann, *Global Physical Climatology* (Academic Press, 1994).
- 480 23. J.-L. Dufresne, S. Bony, An Assessment of the Primary Sources of Spread of Global
481 Warming Estimates from Coupled Atmosphere–Ocean Models. *J. Clim.* **21**, 5135–
482 5144 (2008).
- 483 24. A. Robock, Ice and Snow Feedbacks and the Latitudinal and Seasonal Distribution
484 of Climate Sensitivity. *J. Atmospheric Sci.* **40**, 986–997 (1983).
- 485 25. D. K. Perovich, B. C. Elder, Temporal evolution of Arctic sea-ice temperature. *Ann.*
486 *Glaciol.* **33**, 207–211 (2001).
- 487 26. H. Huwald, L.-B. Tremblay, H. Blatter, A multilayer sigma-coordinate
488 thermodynamic sea ice model: Validation against Surface Heat Budget of the Arctic
489 Ocean (SHEBA)/Sea Ice Model Intercomparison Project Part 2 (SIMIP2) data. *J.*
490 *Geophys. Res. Oceans* **110** (2005).
- 491 27. A. Sirevaag, *et al.*, Mixing, heat fluxes and heat content evolution of the Arctic
492 Ocean mixed layer. *Ocean Sci.* **7**, 335–349 (2011).

- 493 28. M. Steele, W. Ermold, J. Zhang, Arctic Ocean surface warming trends over the past
494 100 years. *Geophys. Res. Lett.* **35** (2008).
- 495 29. V. Ivanov, *et al.*, Arctic Ocean Heat Impact on Regional Ice Decay: A Suggested
496 Positive Feedback. *J. Phys. Oceanogr.* **46**, 1437–1456 (2015).
- 497 30. S. A. Sejas, M. Cai, Isolating the Temperature Feedback Loop and Its Effects on
498 Surface Temperature. *J. Atmospheric Sci.* **73**, 3287–3303 (2016).
- 499 31. F. Massonnet, *et al.*, Arctic sea-ice change tied to its mean state through
500 thermodynamic processes. *Nat. Clim. Change* **8**, 599–603 (2018).
- 501 32. K. E. Taylor, R. J. Stouffer, G. A. Meehl, An Overview of CMIP5 and the
502 Experiment Design. *Bull. Am. Meteorol. Soc.* **93**, 485–498 (2012).
- 503
- 504

Figures

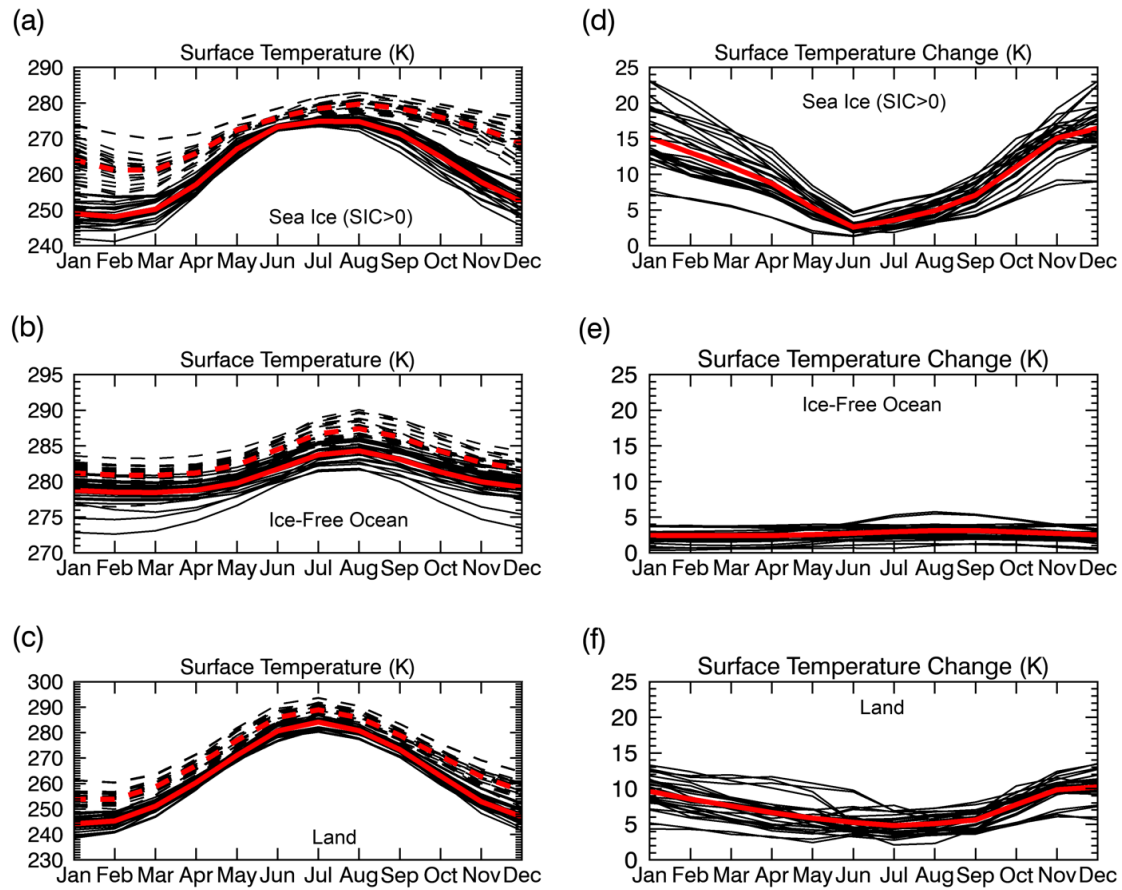


Figure 1. Seasonal Arctic warming by surface type. Climatological seasonal cycle of Arctic (60N-90N) surface skin temperature (K) for the end of the 20th (solid lines) and 21st (dashed lines) centuries projected by CMIP5 historical and RCP8.5 simulations, respectively, for individual CMIP5 models (black lines) and their ensemble mean (red lines) for (a) sea ice, (b) oceanic, and (c) land grid points. The difference between corresponding dashed and solid lines in (a)-(c) is given by (d)-(f), respectively.

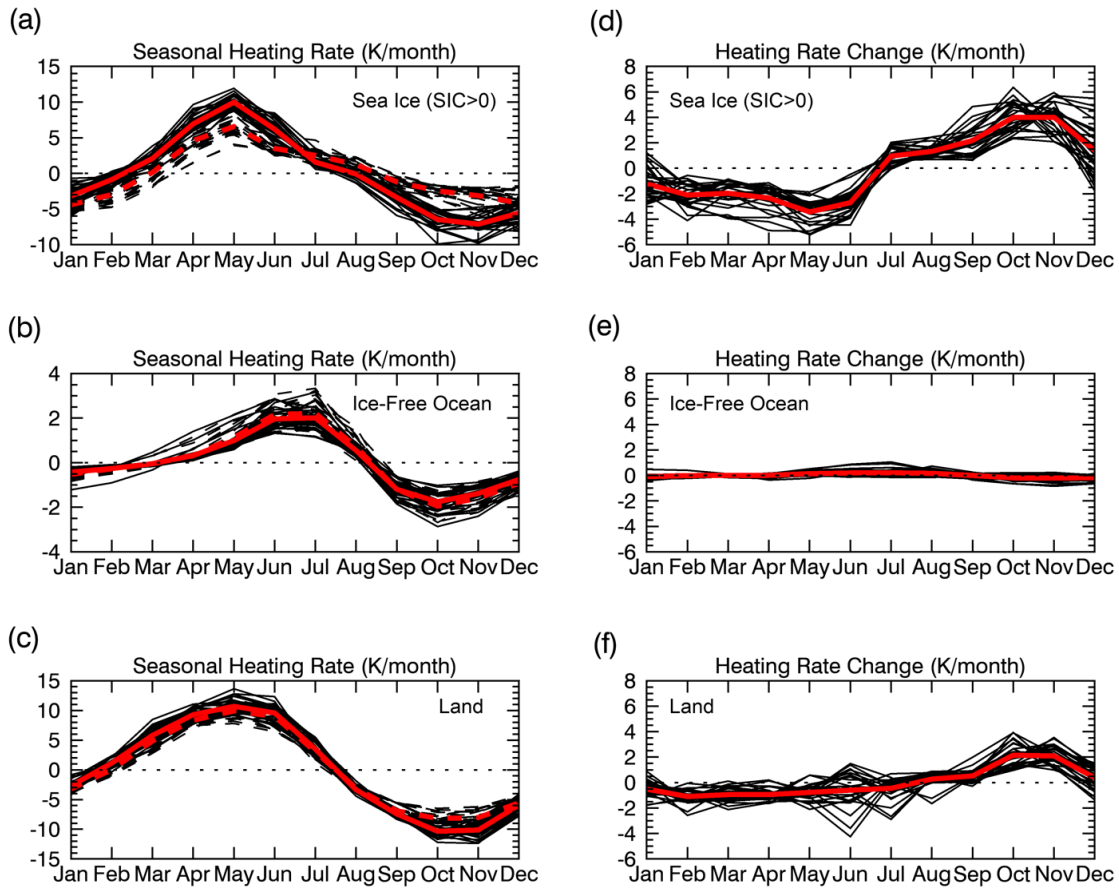


Figure 2. Seasonal heating rate by surface type. Climatological Arctic (60N-90N)

seasonal heating rate (month-to-month; K/month) for the end of the 20th (solid lines) and 21st (dashed lines) centuries projected by CMIP5 historical and RCP8.5 simulations, respectively, for individual CMIP5 models (black lines) and their ensemble mean (red lines) for (a) sea ice, (b) oceanic, and (c) land grid points. The difference between corresponding dashed and solid lines in (a)-(c) is given by (d)-(f), respectively.

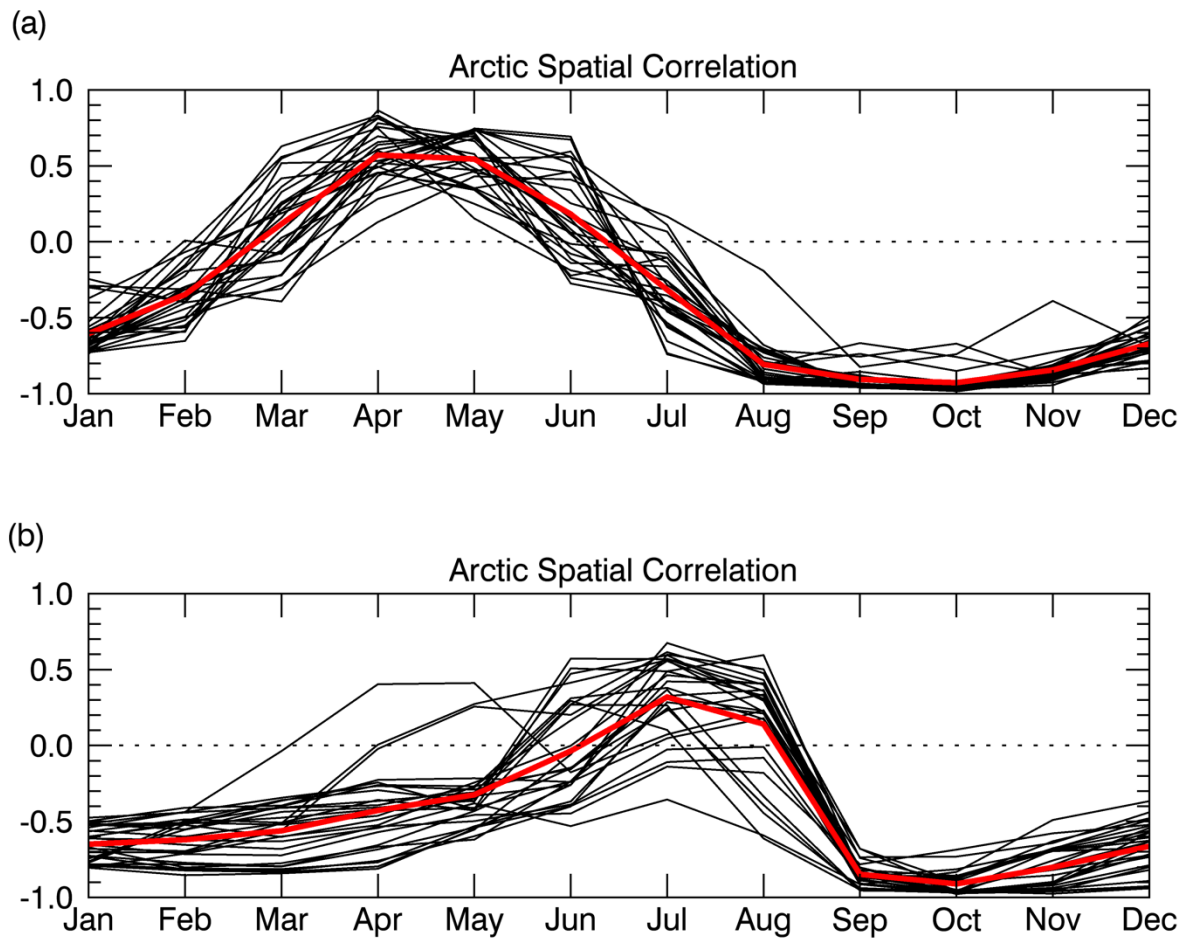


Figure 3. Spatial correlation. (a) Monthly area-weighted spatial correlation between changes in sea ice concentration and surface skin temperature heating rate, and (b) between changes in sea ice concentration and surface skin temperature. Computed for sea ice grid points in the Arctic (between 60N-90N) for individual CMIP5 models (black lines) and their ensemble mean (red line).

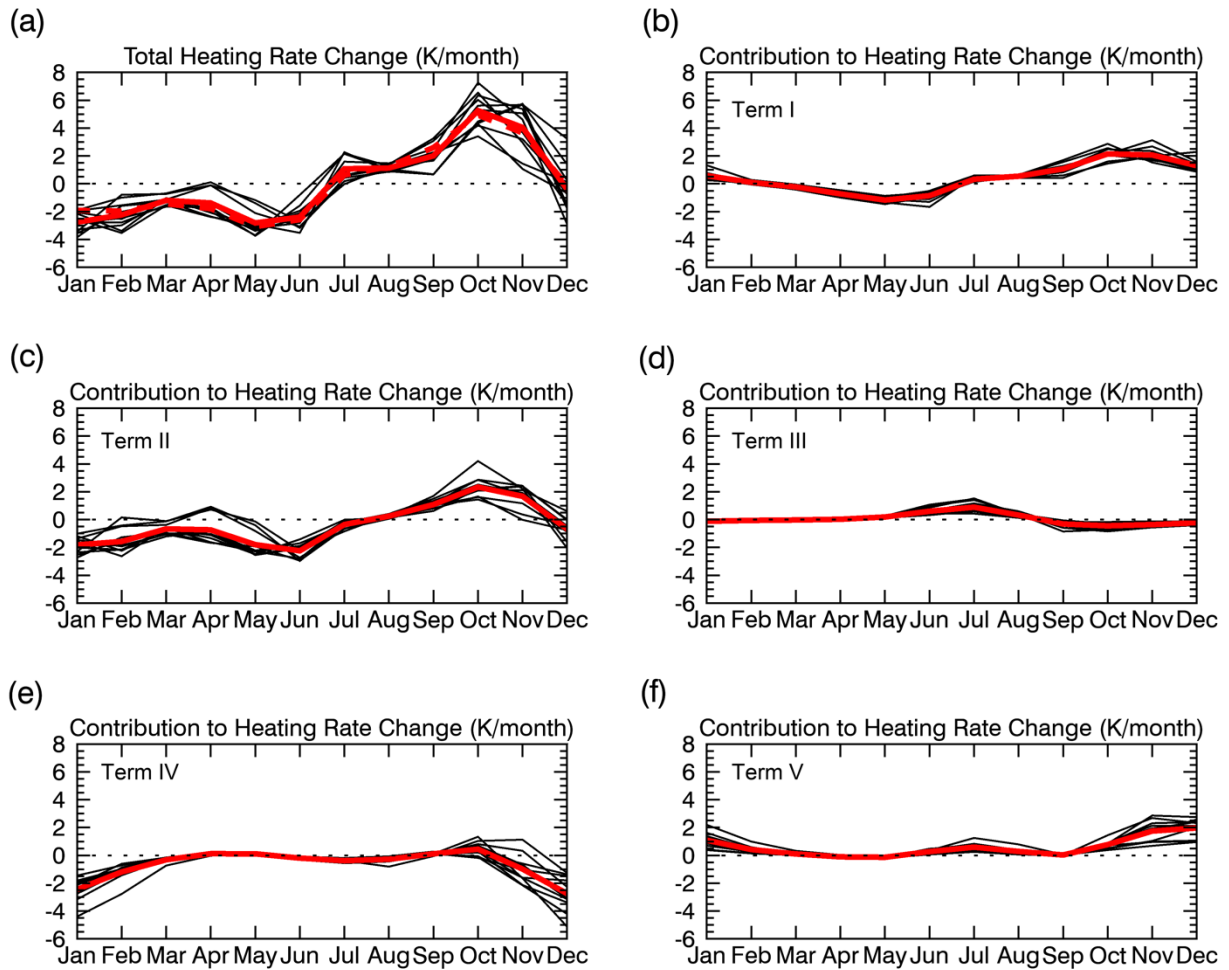


Figure 4. Contributions to the seasonal heating rate change. a) Total change of the seasonal heating rate given by the sum of b-f, where the dashed red line is the actual ensemble mean change of the seasonal heating rate. Contributions to the seasonal heating rate change by the b) sea ice concentration change (term I), c) change of the sea ice surface seasonal heating rate (term II), d) change of the sea surface seasonal heating rate (term III), e) change in the seasonal variation of sea ice concentration (term IV), and f) change in the temperature difference between the sea surface and sea ice surface (term V). Results for individual CMIP5 models are given by the black lines, while the ensemble mean is given by the red lines. Done for Arctic (60N-90N) sea ice grid points.

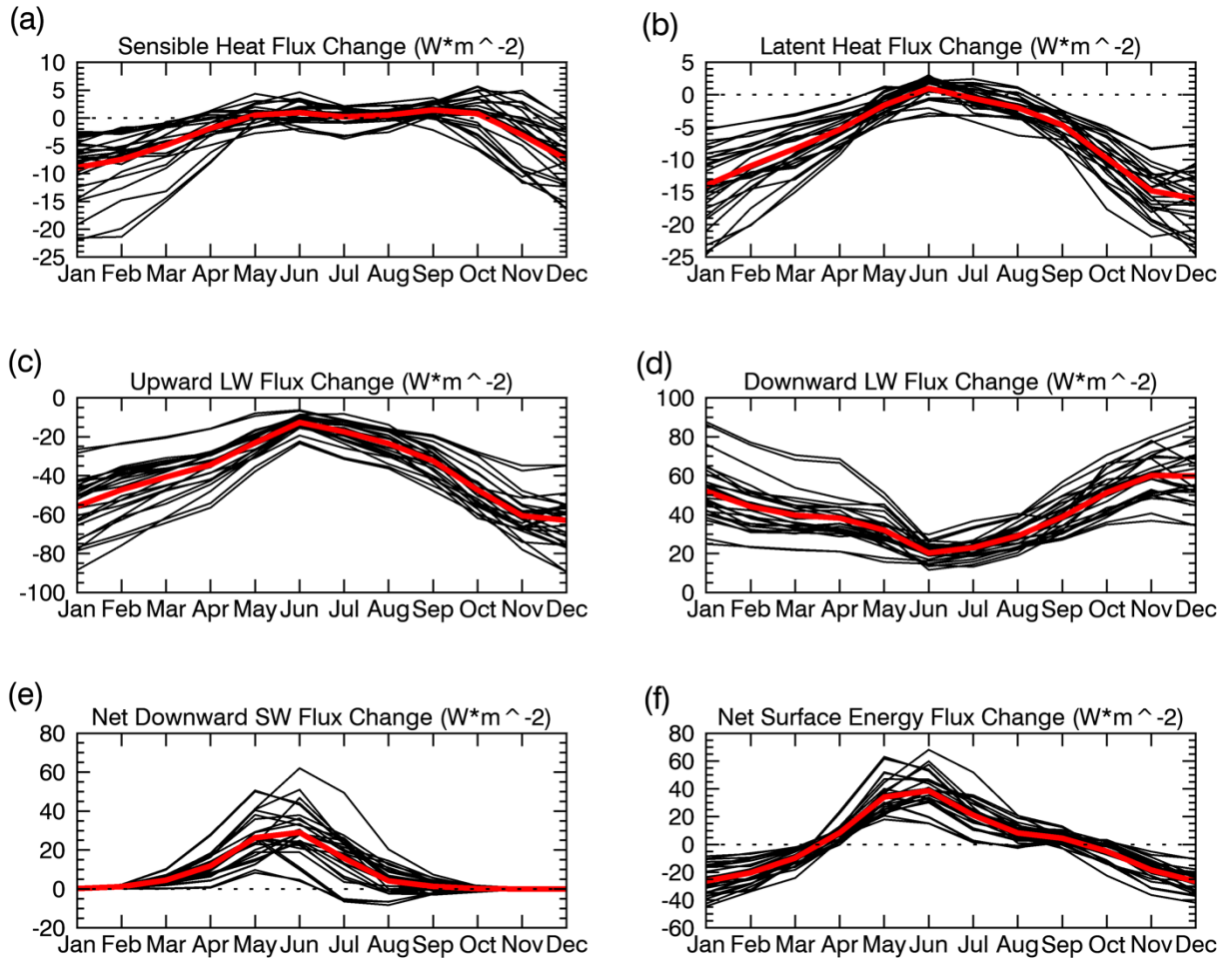


Figure 5. Surface energy budget changes. Changes (W m^{-2}) in a) sensible heat flux, b) latent heat flux, c) upward longwave flux, d) downward longwave flux, e) net downward shortwave flux, and f) the net energy flux (sum of a-e) at the surface for individual CMIP5 models (black lines) and the ensemble mean (red lines) for Arctic (60N-90N) sea ice grid points.

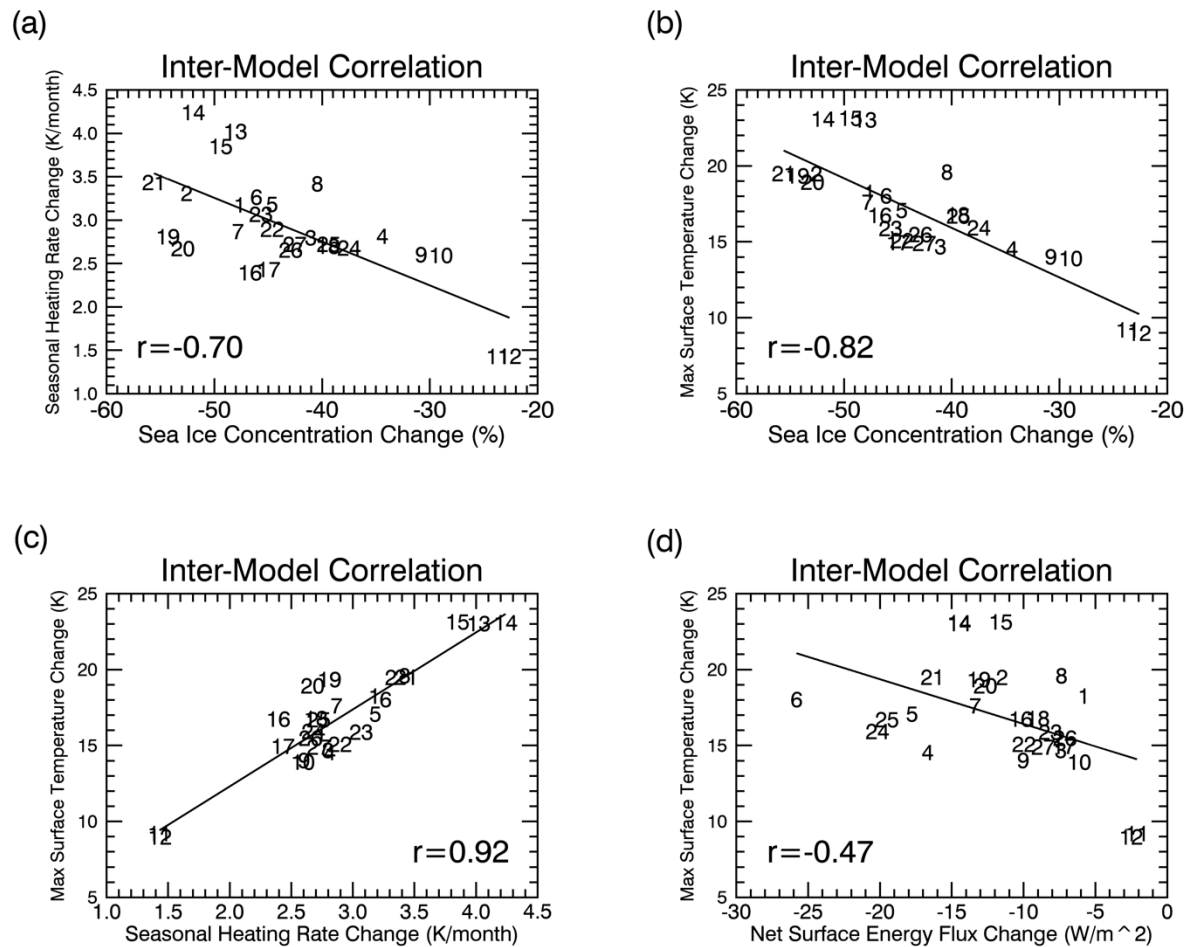


Figure 6. Inter-model Correlations. Correlations across models between (a) SOND sea ice concentration changes and SOND seasonal heating rate changes, (b) SOND sea ice concentration changes and maximum winter warming, (c) SOND seasonal heating rate changes and maximum winter warming, and (d) SOND net surface energy flux changes and maximum winter warming. Computed for Arctic (60N-90N) sea ice grid points.

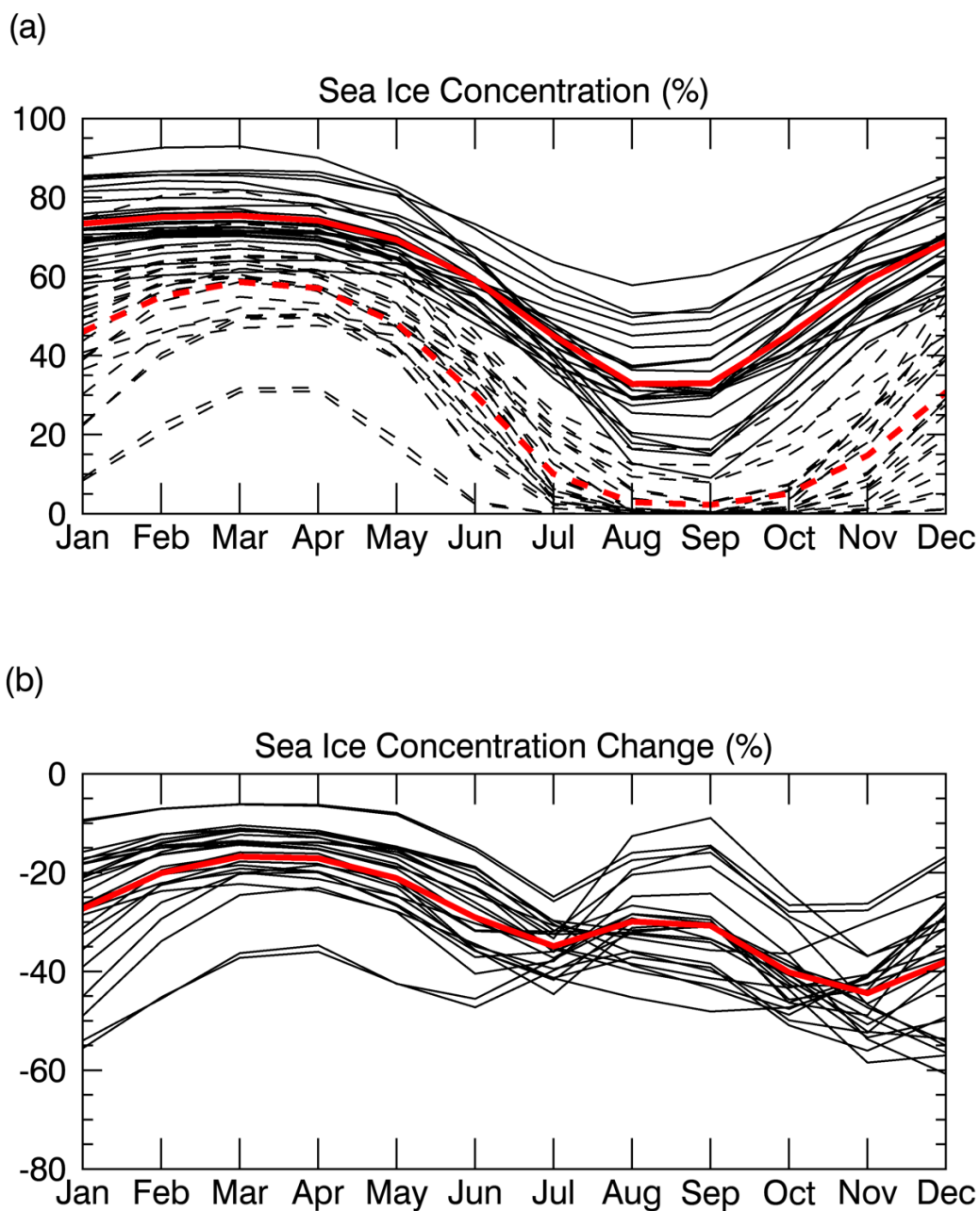
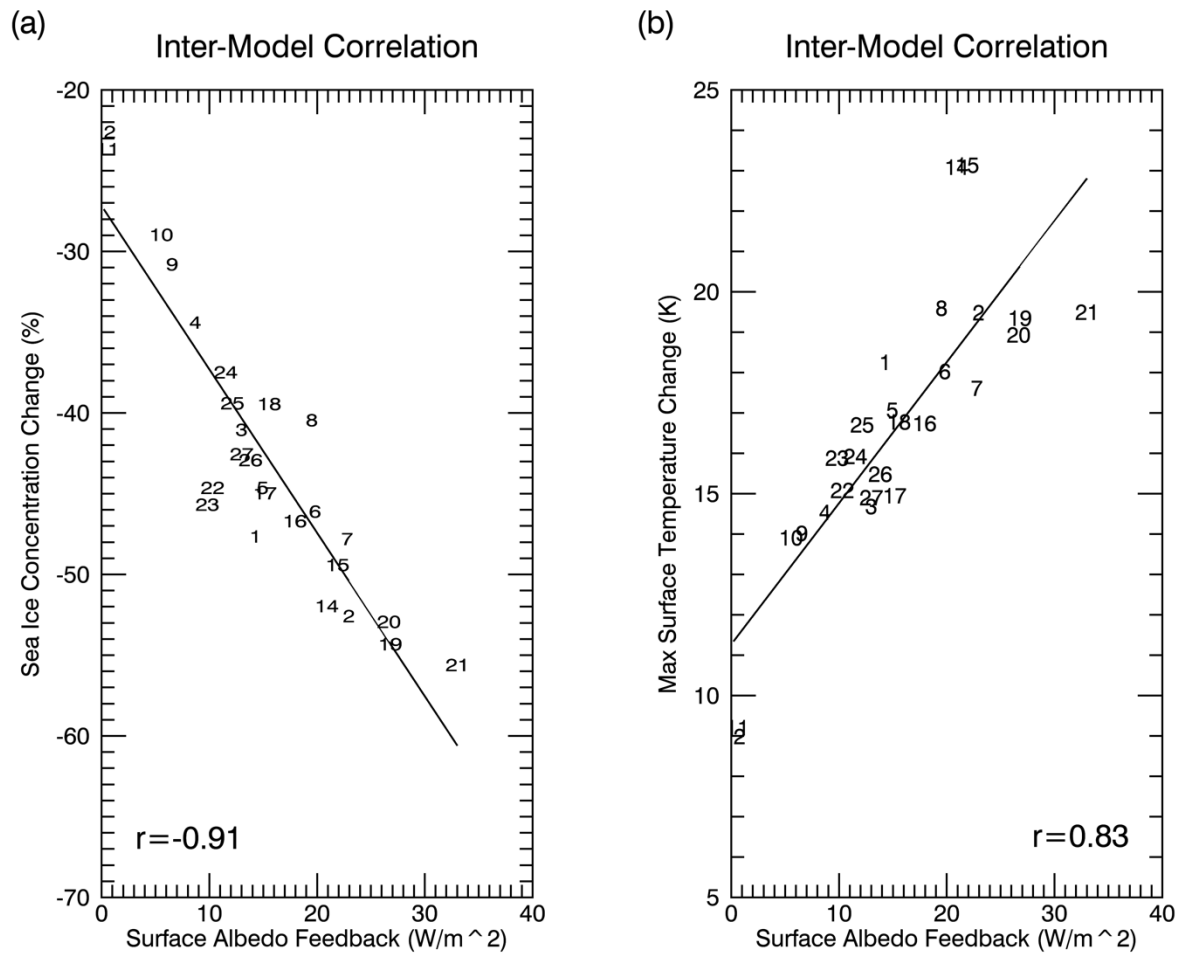
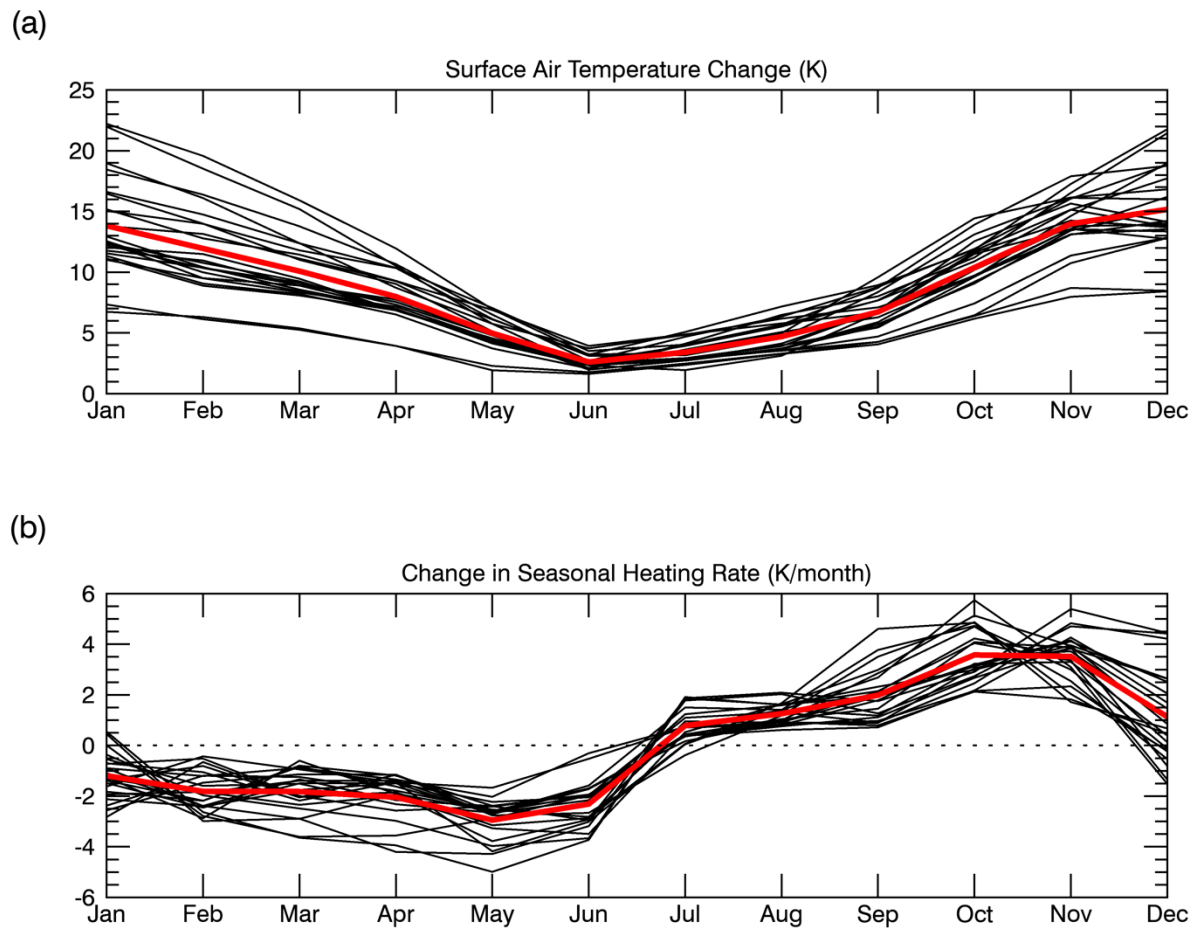


Figure S1. Seasonal sea ice concentration. (a) Arctic (60N-90N) climatological monthly mean sea ice concentration (%) for the end of the 20th (solid lines) and 21st (dashed lines) centuries projected by CMIP5 historical and RCP8.5 simulations, respectively, for individual CMIP5 models (black lines) and their ensemble mean (red lines). (b) Sea ice concentration change (%) given by the difference between corresponding dashed and solid lines in (a). Computed for sea ice grid points.



564

565 **Figure S2. SAF Correlations.** Correlations across the CMIP5 model ensemble between
 566 (a) spring/summer (MAMJJA) surface albedo feedback (SAF) and SOND sea ice
 567 concentration changes and, (b) spring/summer SAF and maximum winter warming.
 568 Computed for Arctic (60N-90N) sea ice grid points.



569

570 **Figure S3. Imprint on Surface Air Temperature.** a) Surface air temperature change
 571 (K) and b) changes to the surface air seasonal heating rate (K/month) for individual
 572 CMIP5 models (black lines) and the ensemble mean (red lines). Done for Arctic (60N-
 573 90N) sea ice grid points.
 574

Model
1. Australian Community Climate and Earth-System Simulator, version 1.0 (ACCESS1.0)
2. Australian Community Climate and Earth-System Simulator, version 1.3 (ACCESS1.3)
3. Community Climate System Model, version 4 (CCSM4)
4. Centro Euro-Mediterraneo per I Cambiamenti Climatici Carbon Earth System Model (CMCC-CESM)
5. Centro Euro-Mediterraneo per I Cambiamenti Climatici Climate Model (CMCC-CM)
6. Centro Euro-Mediterraneo per I Cambiamenti Climatici Climate Model with a resolved Stratosphere (CMCC-CMS)
7. Centre National de Recherches Meteorologiques Coupled Global Climate Model, version 5 (CNRM-CM5)
8. Second Generation Canadian Earth System Model (CanESM2)
9. Goddard Institute for Space Studies Model E2, coupled with the Hybrid Coordinate Ocean Model (GISS-E2-H)
10. Same as above except with interactive terrestrial carbon cycle and oceanic bio-geochemistry (GISS-E2-H-CC)
11. Goddard Institute for Space Studies Model E2, coupled with the Russell ocean model (GISS-E2-R)
12. Same as above except with interactive terrestrial carbon cycle and oceanic bio-geochemistry (GISS-E2-R-CC)
13. Hadley Centre Global Environment Model, version 2 – Atmosphere-Ocean (HadGEM2-AO)
14. Hadley Centre Global Environment Model, version 2 – Carbon Cycle (HadGEM2-CC)
15. Hadley Centre Global Environment Model, version 2 – Earth System (HadGEM2-ES)
16. L’Institut Pierre-Simon Laplace Coupled Model, version 5A, low resolution (IPSL-CM5A-LR)
17. L’Institut Pierre-Simon Laplace Coupled Model, version 5A, mid resolution (IPSL-CM5A-MR)
18. L’Institut Pierre-Simon Laplace Coupled Model, version 5A with a different atmospheric model, low resolution (IPSL-CM5B-LR)
19. Model for Interdisciplinary Research on Climate, Earth System Model (MIROC-ESM)
20. Model for Interdisciplinary Research on Climate, Earth System Model with atmospheric chemistry (MIROC-ESM-CHEM)
21. Model for Interdisciplinary Research on Climate, version 5 (MIROC5)
22. Max Planck Institute Earth System Model, low resolution (MPI-ESM-LR)
23. Max Planck Institute Earth System Model, medium resolution (MPI-ESM-MR)
24. Meteorological Research Institute Coupled Atmosphere-Ocean General Circulation Model, version 3 (MRI-CGCM3)
25. Meteorological Research Institute Earth System Model, version 1 (MRI-ESM1)
26. Norwegian Earth System Model, version 1, medium resolution (NorESM1-M)
27. Same as above except with capability to be fully emission driven (NorESM1-ME)